PROCEEDINGS OF SPIE

SPIEDigitalLibrary.org/conference-proceedings-of-spie

Spatio-temporal optical vortex (STOV) pulses

S. Hancock, S. Zahedpour, A. Goffin, H. Milchberg

SPIE.

Spatio-temporal optical vortex (STOV) pulses

S. W. Hancock, S. Zahedpour, A. Goffin, H. M. Milchberg[1]

Institute for Research in Electronics and Applied Physics, University of Maryland, College Park, Maryland 20740

ABSTRACT

We review highlights of our recent contributions to understanding the propagation dynamics and transverse orbital angular momentum of optical pulses carrying spatiotemporal optical vortices (STOVs). STOVs, which were first observed as an emergent phenomenon in nonlinear self-focusing, were first *linearly* generated using a $4f$ pulse shaper and measured using transient-grating single-shot supercontinuum spectral interferometry (TG-SSSI). That STOV-based transverse orbital angular momentum (OAM) is carried at the single photon level was then confirmed in measurements of OAM conservation in second harmonic generation. Our recent theory for the electromagnetic mode structure and transverse OAM of STOV-carrying pulses in dispersive media predicts half-integer OAM and the existence of a transverse OAM-carrying quasiparticle: the bulk medium STOV polariton.

Keywords: spatio-temporal optical vortices, orbital angular momentum, structured light

1. INTRODUCTION

Optical vortices are electromagnetic field structures characterized by a rotational flow of energy density around a phase singularity, comprising a null in the field amplitude and a discontinuity in the azimuthal phase. In the most common type of optical vortex in optical beams, the azimuthal phase circulation resides in spatial dimensions transverse to the propagation direction. Examples are the well-known orbital angular momentum (OAM) modes [1], typified by Bessel-Gaussian (BG_l) or Laguerre-Gaussian (LG_{pl}) beams with nonzero azimuthal index l. OAM beams have been used in optical trapping [2] and super-resolution microscopy [3], with proposed applications such as turbulence-resilient free-space communications [4,5] and quantum key distribution [6].

Previously, we reported on the experimental discovery and analysis of the spatiotemporal optical vortex (STOV) [7], whose phase winding resides in the spatiotemporal domain. Toroidal STOVs were found to be a universal electromagnetic structure that naturally emerges from arrested self-focusing collapse of short pulses, which occurs, for example, in femtosecond filamentation in air [8,9] or in relativistic self-guiding in laser wakefield accelerators [10]. As this vortex is supported on the envelope of a short pulse, its description is necessarily polychromatic. For femtosecond filamentation in air, a pulse with no initial vorticity collapses and generates plasma at beam center. The ultrafast onset of plasma provides sufficient transient phase shear to spawn two toroidal spatiotemporal vortex rings of topological charge $l = -1$ and $l = +1$ that wrap around the pulse propagation axis. In air, the delayed rotational response of N_2 and O_2 [11] provides additional transient phase shear, generating additional $l = \pm 1$ toroidal STOVs on the trailing edge of the pulse [7]. After some propagation distance and STOV–STOV dynamics, the self-guided pulse is accompanied by the $l = +1$ vortex, which governs the intra-pulse energy flow supporting self-guiding [7].

The requirement of transient phase shear for such nonlinearly generated STOVs suggested that phase shear linearly applied in the spatiospectral domain could also lead to STOVs, and use of a zero dispersion ($4f$) pulse shaper and phase masks have been proposed [12] and first demonstrated [13, 14] for this purpose, later followed by [15]. In this paper, we review our recent results: the generation of free-space propagation of STOVs [14] and their measurement [16], the conservation of OAM in second-harmonic generation from STOVs [17], and the electromagnetic mode structure and transverse OAM of STOVs [18].

A $4f$ pulse shaper can be used to impose STOVs on Gaussian pulses and record in-flight phase and amplitude images of these structures in a single shot using a new diagnostic developed for this purpose. The structures generated are "line-

---

[1] milch@umd.edu; phone 301.405.4816; https://lasermatter.umd.edu

STOVs" as described in [7, 12-18]; the phase circulates around a straight axis normal to the propagation direction and to the spatio-temporal plane. An electric field component of a simple $|l|^{th}$ order line-STOV–carrying pulse of center wavenumber k_0 at position z along the propagation axis (for $|z| << z_R$, the Rayleigh range) can be written as

$$E(\mathbf{r}_\perp, z, \tau) = a\left(\frac{\tau}{\tau_s} + i\, \mathrm{sgn}\,(l)\frac{x}{x_s}\right)^{|l|} e^{ik_0 z} E_0(\mathbf{r}_\perp, z, \tau) = A(x,\tau)e^{il\Phi_{s-t}}e^{ik_0 z}E_0(\mathbf{r}_\perp, z, \tau), \tag{1}$$

where $\mathbf{r}_\perp = (x, y)$, $\tau = t - z/v_g$ is a time coordinate local to the pulse, v_g is the group velocity, τ_s and x_s are temporal and spatial scale widths of the STOV, $\Phi_{s-t}(x,\tau)$ is the space-time phase circulation in $x - \tau$ space, $l = \pm 1, \pm 2, \ldots$, $A(x,\tau) = a((\tau/\tau_s)^2 + (x/x_s)^2)^{|l|/2}$, $a = \sqrt{2}\,((x_0/x_s)^2 + (\tau_0/\tau_s)^2)^{-1/2}$ for $l = \pm 1$, and E_0 is the envelope of the STOV-free near-Gaussian pulse input to the $4f$ shaper, where x_0 and τ_0 are its spatial and temporal widths. Here a is a normalization factor ensuring that pulse energy is conserved through the shaper: $\int d^2\mathbf{r}_\perp d\tau|E|^2 = \int d^2\mathbf{r}_\perp d\tau|E_0|^2$.

2. GENERATION AND MEASUREMENT OF STOVs

The pulse shaper imposes a line-STOV on an input Gaussian pulse (50 fs, 1.5–20 μJ) using a $2\pi l$ spiral transmissive phase plate (with $l = +1, -1$) or a π-step plate at the shaper's Fourier plane (common focus of the cylindrical lenses). The vertical and horizontal axes on the phase masks lie in the spatial (x) and spectral (ω) domains. The phase plate orientations are shown in the figure, where for the step plate, the adjustable angle α is with respect to the spectral (dispersion) direction. While the shaper imposes a spatiospectral (x, ω) phase at the phase plate, leading to a spatiotemporal (x, τ) pulse immediately at its output at the exit grating (near field), our desired spatial effects appear in the far field of the shaper, where the desired STOV-carrying pulse emerges.
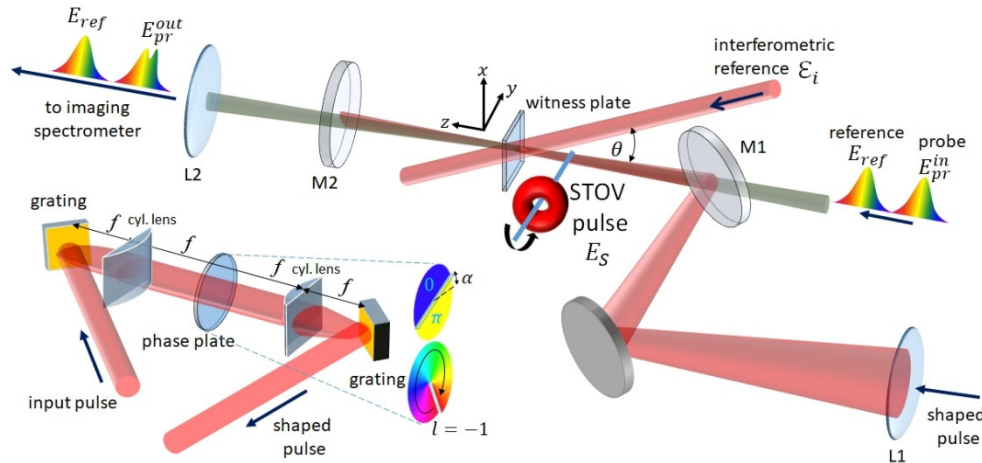

Figure 1. <u>Top:</u> Setup for transient grating single-shot spectral interferometry (TG-SSSI) [16]. The STOV-carrying pump pulse (center wavelength $\lambda_0 =$800nm) at the output of a $4f$ pulse shaper is focused (~1.5 μJ) or imaged (~20 μJ) into a 500 μm thick fused silica witness plate. The pump pulse energy is kept sufficiently low so that the STOV pulse propagates nearly linearly in the plate. A interferometric probe pulse $\mathcal{E}_i$ ($\lambda_0 = $795nm, 2 nm bandwidth) crosses the STOV pulse direction at angle $\theta = 6°$, forming a transient grating with modulations $f(x,\tau) = \cos(kx\sin\theta + \Delta\Phi(x,\tau))$, where the symbols are defined in the main text and reference coordinates are shown next to the witness plate, and $\Delta\Phi(x,\tau)$ is the spatiotemporal phase to be extracted . The transient grating is probed by SSSI [19], which uses ~1.5 ps long chirped supercontinuum reference and probe pulses E_{ref} and E_{pr} ($\lambda_0\sim$575 nm). The result is single-shot time and space resolved images of amplitude and phase of STOV-carrying pulses. Extracted is Bottom<u>left:</u> Cylindrical lens-based $4f$ pulse shaper [12-14] for imposing a line-STOV on a 45 fs, λ=800nm input pulse. A thin phase plate is inserted in the Fourier plane at the common focus of the cylindrical lenses. We used spiral phase plates ($l = 1$, $l = -1$) and a π-step plate, all etched on fused silica, where the π-step angle α and the spiral orientation (for $l = -1$) are also shown. The $l = \pm 1$ plates have 16 levels (steps). Shaper gratings: 1200 line/mm, cylindrical lenses: focal length 20cm.

Here, we project to the far field by lens-focusing the STOV output pulse from the shaper into a 500 μm thick fused silica "witness plate", whereupon it is measured using transient grating single-shot supercontinuum spectral interferometry (TG-SSSI) [16].

Figure 2 shows typical TG-SSSI measurement results. Row (a) shows the pulse with no phase plate in the pulse shaper. This is the far field output of the shaper as measured by TG-SSSI in the witness plate. The temporal leading edge is at $\tau < 0$. The left column plots the extracted $\Delta\phi(x,\tau) \propto |E_s(x,\tau)|^2 + 2|E_s||\mathcal{E}_i|f(x,\tau)$, where $|E_s|^2 \propto I_s$ is the 1D space + time pump intensity envelope and $f(x,\tau) = \cos(2k_w x \sin(\theta_w/2) + \Delta\Phi(x,\tau))$ where $k_w = n_0 k$ is the pump central wavenumber in the witness plate and θ_w is the angle between E_s and $\mathcal{E}_i$ inside the witness plate (see Fig. 1 and caption). The fringes are removed with a low pass filter, yielding $I_S(x,\tau)$ in the next column, while in the third column, a high pass filter leaves the fringe image $f(x,\tau)$. The far right column shows the extracted spatio-temporal phase $\Delta\Phi(x,\tau)$. It is seen that the pulse envelope I_S closely agrees with the 50 fs pulse input to the shaper, and that $\Delta\Phi(x,\tau)$ is weakly parabolic in time (small chirp) and relatively flat in space.
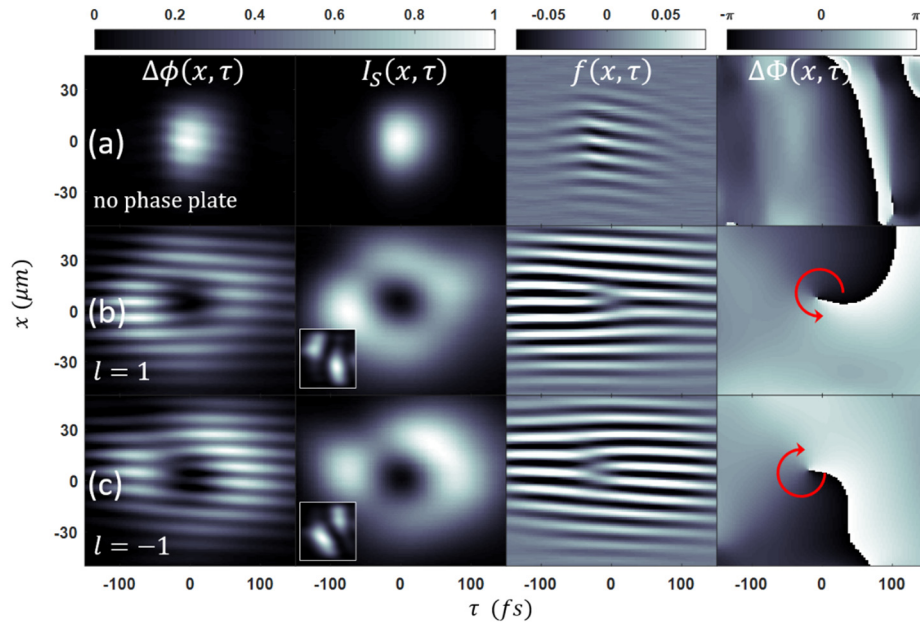

Figure 2. (a) Output of pulse shaper with no phase plate. The 50 fs input pulse, with a weakly parabolic temporal phase, is recovered. (b, c) Intensity and phase of pulse in far-field of pulse shaper with $l = 1$ and $l = -1$ spiral phase plates. White-bordered insets: pulse shaper near-field intensity images. The red arrows show the direction of phase circulation. Headings of each column are described in the text. In all panels, the temporal leading edge of the pulse is on the left ($\tau < 0$), so propagation is right-to-left. The pulse energy for the three far field cases above is ~1μJ. For the near field cases (insets), the pulse energy is increased to ~20μJ to offset the reduced signal due to magnification.

The slight curvature of the fringes of $f(x,\tau)$ seen in Fig. 2 is attributed to spectral phase mismatch between E_s and $\mathcal{E}_i$. One form of line-STOV-carrying pulse can be generated with a spiral phase plate in the pulse shaper. For a $l = 1$ plate, row (b) of Fig. 2 shows, as in (a), the various extractions from TG-SSSI. The presence of a spatio-temporal phase singularity is evident from the characteristic forked pattern in $f(x,\tau)$. The spatio-temporal envelope $I_S(x,\tau)$ and phase $\Delta\Phi(x,\tau)$ of the STOV are shown in the second and fourth columns, where the pulse appears as an "edge-first flying donut" with a 2π phase circulation around the phase singularity at the donut null. Using a $l = -1$ plate (flipping the $l = 1$ plate) generates the opposite spatio-temporal phase circulation, as seen in row (c). The small insets in (b) and (c) show the corresponding near-field intensity envelopes from the shaper, consisting of 2 lobes separated by a space-time diagonal.

3. OAM CONSERVATION IN SECOND HARMONIC GENERATION OF STOVs

Because OAM in standard beams (such as Laguerre-Gaussian) is conserved under second harmonic generation (SHG) [20], it is of significant interest to test this with STOV pulses. Given perfect phase matching in the undepleted pump regime, the process of second harmonic generation (SHG) involving monochromatic and polychromatic beams yields a nonlinear polarization and second harmonic field output proportional to the square of the input field [21]. As applied to the fundamental STOV pulse of Eq. (1), the same process would give

$$E_S^{2\omega}(\mathbf{r}_\perp, z, \tau) \propto a^2 \left(\frac{\tau}{\tau_s} \pm i\,\mathrm{sgn}(l)\frac{x}{x_s}\right)^{2|l|} E_0^2(\mathbf{r}_\perp, z, \tau), \tag{2}$$

$$= A^2(x, \tau)e^{i2l\Phi_{s-t}}E_0^2(\mathbf{r}_\perp, z, \tau)$$

Note that the propagation phase factor $e^{ik_0 z}$ in Eq. (1) contributes a purely spatial phase shift, affecting only extrinsic orbital angular momentum; it does not contribute to the SHG process. Equation (2) predicts that the frequency doubled pulse will have twice the topological charge and angular momentum as the fundamental STOV-carrying pulse.

TG-SSSI measurements of the fundamental and SHG STOV pulses (generated by placing a 100μm thick BBO crystal at the exit of the pulse shaper) are shown in Fig. 3, where the red colourmap panels of (a) show the spatiotemporal intensity $I_S(x, \tau)$ and phase $\Delta\Phi(x, \tau)$ of the fundamental $l = +1$ STOV $E_S(x, \tau)$ at the near-field output of the $4f$ pulse shaper (here using a π-step plate). $I_S(x, \tau)$ has the characteristic edge-first flying donut profile, with the pulse propagating right-to-left, while $\Delta\Phi(x, \tau)$ is a single 2π phase winding centred at $(x, \tau) = (0,0)$. The dip in intensity near $x = -60\mu m$ in Fig. 3(a) is due to scattering off the π-step of the phase plate. Figure 3(b), in blue colormap, shows the measured spatiotemporal intensity $I_S^{2\omega}(x, \tau)$ and phase $\Delta\Phi^{2\omega}(x, \tau)$ of $E_S^{2\omega}(x, \tau)$. Instead of a single $l = +2$ STOV , for which $I_S^{2\omega}(x, \tau)$ would have a single intensity null and $\Delta\Phi^{2\omega}(x, \tau)$ would have a 4π phase winding, we see that $I_S^{2\omega}(x, \tau)$ and $\Delta\Phi^{2\omega}(x, \tau)$ show two spatiotemporally offset vortices, embedded in the second harmonic pulse, around whose centers are two 2π phase windings. This constitutes two $l = +1$ STOVs, and thus energy conservation dictates that the $E_S^{2\omega}$ pulse carries, on average, twice the OAM per photon of the fundamental E_S. The spatiotemporal splitting of the STOV in $E_S^{2\omega}$ is due to (1) group velocity mismatch GVM ($= 1/v_g^{(2\omega)} - 1/v_g^{(\omega)}$) between the E_S^ω and $E_S^{2\omega}$ pulses in the BBO crystal [17] and (2) group delay dispersion (GDD) in both the BBO crystal and imaging lens.
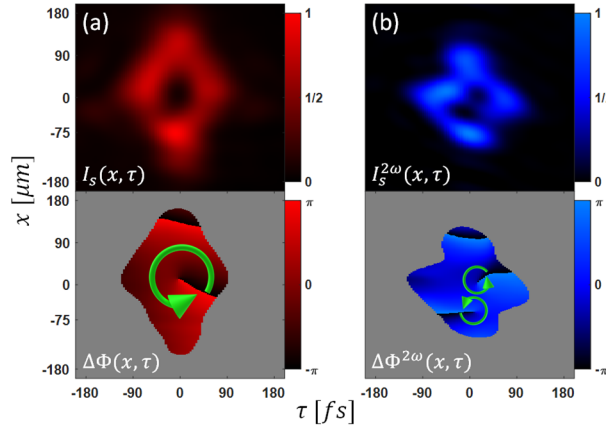

Figure 3. TG-SSSI measurements of fundamental and SHG STOVs. (a) Top: Intensity profile $I_S(x, \tau)$ of fundamental $l = +1$ STOV; Bottom: spatiotemporal phase $\Delta\Phi(x, \tau)$ showing one 2π winding. (b) Top: SHG output pulse $I_S^{2\omega}(x, \tau)$ showing two donut holes embedded in pulse; Bottom: spatiotemporal phase profile $\Delta\Phi^{2\omega}(x, \tau)$ showing two 2π windings. Phase traces are blanked in regions of negligible intensity, where phase extraction fails. These images represent 500 shot averages: the extracted phase shift from each spectral interferogram is extracted, then the fringes of each frame (shot) are aligned and averaged, then the phase map is extracted [16].

The question of whether photons in an ultrashort STOV pulse individually carry transverse OAM is difficult to answer experimentally in linear optics: one would need to attenuate the pulse and somehow examine the statistical spatiotemporal distribution of photons. However, this question is more easily answered using nonlinear optics. The conservation of photon number implied by the Manley-Rowe relations for SHG, $2\,d/dz\left(I^{(\omega)}/\hbar\omega\right) = d/dz\left(I^{(2\omega)}/\hbar\omega\right)$ [21], implies that, *on average*, photons at the second harmonic carry twice the OAM of photons at the fundamental. However, because SHG is fundamentally a quantum mechanical process involving light-matter interactions of the quantized electromagnetic field, and because all photons in the STOV pulse from our pulse shaper carry the same bandwidth, polarization, and spatiotemporal phase, we conclude that energy and angular momentum conservation in the SHG process holds at the individual photon level—and that photons in STOV-carrying pulses have OAM orthogonal to their direction of propagation. It is also worth noting that if we take a STOV pulse of the type generated here, and greatly attenuate it to just

a few photons, the uncertainty relations $\Delta k_x \Delta x \geq 1/2$ and $\Delta k_\xi \Delta \xi \geq 1/2$ ensure that a photon with STOV OAM could be found anywhere in the transverse and longitudinal extent of the pulse, and could have any frequency consistent with the bandwidth.

4. MODE STRUCTURE AND ORBITAL ANGULAR MOMENTUM OF STOVs

Next, we present a review of our modal theory of STOVs and transverse OAM [22]. STOV-supporting modal solutions of the paraxial wave equation, accounting for possible dispersion in the propagation medium, have been found from the Fourier transformed wave equation for a uniform isotropic medium with dielectric function $\varepsilon(\omega)$ and wavenumber given by $k^2(\omega) = \omega^2 \varepsilon(\omega)/c^2$,

$$\left(\nabla_\perp^2 + \frac{\partial^2}{\partial z^2} + k^2(\omega) \right) \widetilde{\mathcal{A}}(\mathbf{r}_\perp, z, \omega) = 0, \tag{3}$$

where $\widetilde{\mathcal{A}}$ is the $t \to \omega$ Fourier-transformed vector potential, pulse propagation is along $\hat{\mathbf{z}}$, $\mathbf{r}_\perp$ represents transverse coordinates orthogonal to $\hat{\mathbf{z}}$, and $\nabla_\perp^2$ is the corresponding transverse Laplacian. After assuming a slowly varying envelope and adopting the paraxial approximation, expanding around the central wavenumber, assuming the bandwidth is not too large and making the substitutions $\xi = v_g t - z$ and $\beta_2 = v_g^2 k_0 k_0''$, we get for the paraxial spatiotemporal wave equation [22],

$$2ik_0 \frac{\partial}{\partial z} \mathbf{A}(\mathbf{r}_\perp, \xi; z) = \left(-\nabla_\perp^2 + \beta_2 \frac{\partial^2}{\partial \xi^2} \right) \mathbf{A}(\mathbf{r}_\perp, \xi; z) = H\mathbf{A}(\mathbf{r}_\perp, \xi; z), \tag{4}$$

Here, ξ is a (local time-like) space coordinate in the frame of the pulse, β_2 is the dimensionless group velocity dispersion (GVD), $\mathbf{A}$ is the slowly varying envelope, $H = (-\nabla_\perp^2 + \beta_2 \partial^2/\partial \xi^2)$ is the spacetime propagator, and we separate z with a semicolon as it plays the role of a time-like running parameter.

Next, we assume a uniformly polarized beam $\mathbf{A}(\mathbf{r}_\perp, \xi; z) = A(\mathbf{r}_\perp, \xi; z)\hat{\mathbf{e}}$, where $\hat{\mathbf{e}}$ is the complex polarization (here we take $\hat{\mathbf{e}} = \hat{\mathbf{y}}$ as in our experiments [14], where there are no effects of spin angular momentum [23,24]), and find modal solutions to Eq. (4) for $\mathbf{r}_\perp = (x, y)$:

$$A_{mpq}(x, y, \xi; z) = A_{mpq}^{(0)} u_m^x(x; z) u_p^y(y; z) u_q^\xi(\xi; z), \tag{5}$$

where

$$u_q^\xi(\xi; z) = \frac{C_q}{\sqrt{w_\xi(z)}} H_q\left(\frac{\sqrt{2}\,\xi}{w_\xi(z)} \right) e^{-\xi^2/w_\xi^2(z)} e^{-\frac{ik_0 \xi^2}{2\beta_2 R_\xi(z)}} e^{i\left(q+\frac{1}{2}\right)\psi_\xi(z)}, \tag{6a}$$

and

$$u_m^x(x; z) = \frac{C_m}{\sqrt{w_x(z)}} H_m\left(\frac{\sqrt{2}\,x}{w_x(z)} \right) e^{-x^2/w_x^2(z)} e^{\frac{ik_0 x^2}{2R_x(z)}} e^{-i\left(m+\frac{1}{2}\right)\psi_x(z)}, \tag{6b}$$

Here, $C_m = \left(\frac{2}{\pi}\right)^{\frac{1}{4}} (2^j\, m!)^{-\frac{1}{2}}$, H_m is a Hermite polynomial of order m, $w_x(z) = w_{0x}(1 + (z/z_{0x})^2)^{1/2}$, $R_x(z) = z(1 + (z_{0x}/z)^2)$, $\psi_x(z) = \tan^{-1}(z/z_{0x})$, and $z_{0x} = k_0 w_{0x}^2/2$ is the x-based Rayleigh range. The expression for $u_p^y(y)$ is identical to Eq. (6b) with the substitution $x \to y$ everywhere. Associated with $u_q^\xi(\xi; z)$ is $z_{0\xi} = k_0 w_{0\xi}^2/2|\beta_2|$, $w_\xi(z) = w_{0\xi}(1 + (z/z_{0\xi})^2)^{1/2}$, $R_\xi(z) = z(1 + (z_{0\xi}/z)^2)$, and $\psi_\xi(z) = \text{sgn}(\beta_2)\tan^{-1}(z/z_{0\xi})$. The quantities $w(z)$, $R(z)$ and $\psi(z)$ express the z-variation in beam size, phase front curvature and Gouy phase shift as they do for standard transverse modes, except that here they also apply in the ξ domain.

The "spot sizes" w_{0x}, w_{0y}, and $w_{0\xi}$ describe the transverse space and temporal shape of the beam envelope of the lowest order mode $((m, p, q) = (0,0,0))$ at $z = 0$, $A_{000}(x, y, \xi; z = 0) = A_{000}^{(0)} e^{-(x^2/w_{0x}^2 + y^2/w_{0y}^2)} e^{-\xi^2/w_{0\xi}^2}$, which approximates the input beam to our pulse shaper. The effective wavenumber k_0/β_2 associated with $u_q^\xi(\xi)$ accounts for the different rate of spreading in temporal dispersion compared to transverse beam diffraction. We have allowed the beam to have elliptical

envelopes in both the $x - y$ (space) and $x - \xi$ (spacetime) planes, and different phase curvatures in x, y, and ξ. The choice of HG basis functions for the solution of Eq. (4) is motivated by our experimental generation of STOV-carrying pulses using a $4f$ pulse shaper [12-14], which imposes rectilinearly-oriented ellipticity and astigmatism in both the space and spacetime domains.

In vacuum or in the very dilute medium (air) of the experiments of [14], $\beta_2 = 0$ and $v_g = c$, $u_q^\xi(\xi; z = 0) = H_q(\sqrt{2}\,\xi/w_{0\xi})e^{-\xi^2/w_{0\xi}^2}$, and Eq. (1) can be represented as a linear combination of spacetime modes (Eqs. (6a), (6b)) at $z = 0$:

$$A_\alpha^{l=\pm 1}(x, y, \xi; z = 0) = A_0 u_0^y(y; 0)\left(u_0^x(x; 0)u_1^\xi(\xi; 0) \pm i u_1^x(x; 0)u_0^\xi(\xi; 0)\right). \tag{7}$$

Given this initial STOV field at $z = 0$, the propagator $H = (-\nabla_\perp^2 + \beta_2\,\partial^2/\partial\xi^2)$ of Eq. (4) generates the full z-dependent evolution

$$A_\alpha^{l=\pm 1}(x, y, \xi; z) = A_0 u_0^y(y; z)\left(u_0^x(x; z)u_1^\xi(\xi; z) \pm i u_1^x(x; z)u_0^\xi(\xi; z)\right). \tag{8}$$

For the case $w_{0x} = w_{0\xi}$ ($\alpha \equiv w_{0\xi}/w_{0x} = 1$), the factor $u_0^x(x; z)u_1^\xi(\xi; z) \pm i u_1^x(x; z)u_0^\xi(\xi; z)$ is analogous to the superposition of the 0th and 1st order Hermite-Gaussian transverse modes (HG_0 and HG_1) to give the Laguerre-Gaussian spatial mode $LG_{space}^{0\pm 1} = HG_0(x)HG_1(y) \pm iHG_1(x)HG_0(y)$. In our experiments, the y-dependent beam envelope shape, aside from transverse diffractive spreading, is preserved in propagation. So, we henceforth neglect y variations in the beam by setting $y = 0$, noting that any 3D mode can be constructed by multiplying the (x, ξ)-dependent results by $u_n(y; z)$.

We now examine the STOV angular momentum, $\hat{\mathbf{y}}L_y$, which is orthogonal to the $x - \xi$ plane of spatiotemporal phase circulation. First, we must find the appropriate angular momentum operator L_y. To do so, we consider Eq. (4) along with the conservation of energy density flux $\mathbf{j}$ [25], $\partial|A|^2/\partial z = -\nabla \cdot \mathbf{j}$, where $\mathbf{j} = \mathbf{j}_\perp + \mathbf{j}_\parallel$, $\mathbf{j}_\perp = -i(2k_0)^{-1}(A^*\nabla_\perp A - A\nabla_\perp A^*)$ and $\mathbf{j}_\parallel = i\beta_2(2k_0)^{-1}[A^*(\partial/\partial\xi)A - A(\partial/\partial\xi)A^*]\hat{\boldsymbol{\xi}}$, where $\hat{\boldsymbol{\xi}}$ is a unit vector along increasing ξ. This gives $\mathbf{j} = k_0^{-1}|A|^2(\nabla_\perp\Phi - \beta_2(\partial\Phi/\partial\xi)\,\hat{\boldsymbol{\xi}}) = k_0^{-1}|A|^2\nabla_{st}\Phi$, where $A = |A|e^{i\Phi}$ and $\nabla_{st} \equiv \nabla_\perp - \hat{\boldsymbol{\xi}}\beta_2(\partial/\partial\xi)$ is the spacetime gradient. Therefore, the spacetime linear momentum operator is $\hat{\mathbf{p}} = -i\nabla_{st}$, giving $L_y = (\hat{\mathbf{r}} \times \hat{\mathbf{p}})_y = (-i\mathbf{r} \times \nabla_{st})_y = -i(\xi\,\partial/\partial x + x\beta_2\,\partial/\partial\xi)$.

To calculate the STOV OAM associated with $A(\rho, y, \Phi; z)_{(l=\pm 1)}$, we note that it is sufficient to do so at the beam waist $z = 0$. This is because $\langle L_y \rangle$ is invariant with propagation, namely $(d/dz)\langle L_y \rangle = i(2k_0)^{-1}\langle [H, L_y] \rangle = 0$, owing to the fact that $[H, L_y] = 0$ [22]; L_y commutes with the propagation operator, as it should for a conserved OAM quantity. It is straightforward to show that $[H, L_y] = 0$ even under non-paraxial conditions. This greatly simplifies the calculation, especially for non-zero β_2, where we consider the beam waist to be placed just inside the material interface ($z = 0^+$) without additional chirp from the material yet induced.

In spacetime polar coordinates ($x = \rho\cos\Phi$, $\xi = \rho\sin\Phi$), the STOV field at $z = 0$ for general l, α can be written as

$$\begin{aligned}A_\alpha^l &= A_\alpha^l(\rho, y = 0, \Phi, z = 0) \\ &= A_0\left(\frac{\rho}{w_{0\xi}}\right)^{|l|}\exp\left(-\frac{\rho^2}{w_{0\xi}^2}(\cos^2\Phi + \alpha^2\sin^2\Phi)\right)(\cos\Phi + i\alpha\,\mathrm{sgn}(l)\sin\Phi)^{|l|}.\end{aligned} \tag{9}$$

It is then straightforward to show that the expectation value of the intrinsic transverse OAM is

$$\langle L_y \rangle = \langle A_\alpha^l | L_y | A_\alpha^l \rangle = \frac{1}{2}l\left(\alpha - \frac{\beta_2}{\alpha}\right), \tag{10}$$

where $\langle L_y \rangle$ depends explicitly on topological charge l, STOV eccentricity α and material dispersion β_2 [22]. This is a remarkable result, for which we first consider the case $\alpha = 1$, a space-time symmetric STOV. For the case of vacuum ($\beta_2 = 0$), $\langle L_y \rangle = l/2$: STOV OAM is quantized in half integer units. For dispersive media ($\beta_2 \neq 0$), a quantum interpretation of the role of β_2 is strongly suggested, where one might consider the material disturbance induced by a STOV-encoded photon field as a new type of quasiparticle, a "STOV polariton".
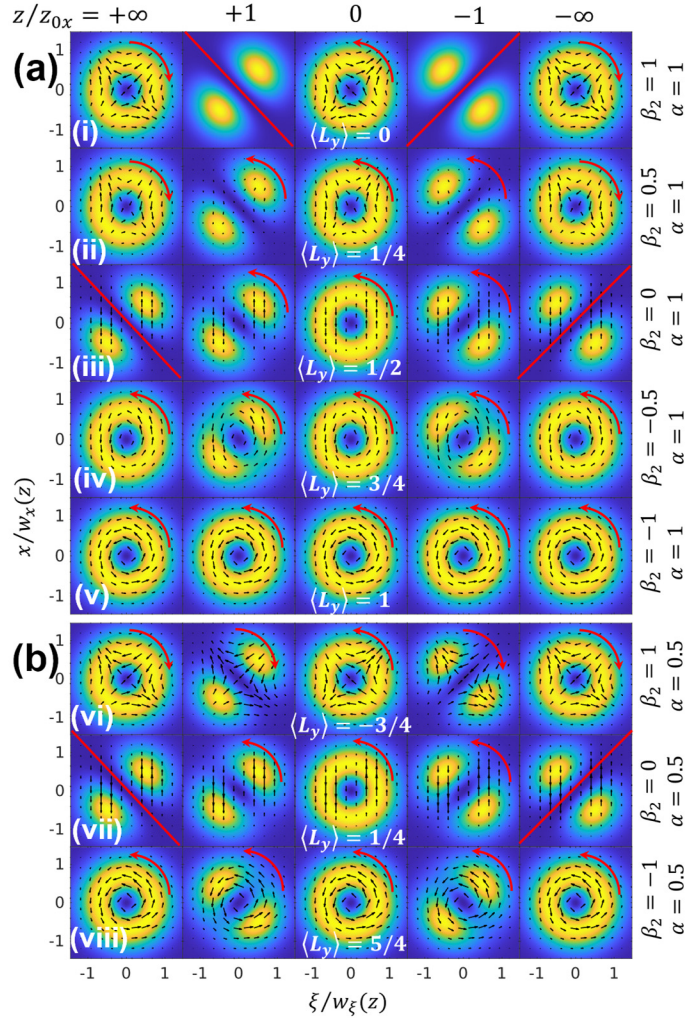
Figure 4. (a) Plots of STOV intensity $\left|A_{\alpha=1}^{l=1}(x, y=0, \xi; z)\right|^2$ and energy density flux $\mathbf{j}$ (depicted by overlaid arrows), computed using Eq. (9) for $l = 1$, $\alpha = 1$ and $\beta_2 = 1,\ 0.5,\ 0, -0.5, -1$. The purely diffractive contributions to $\mathbf{j}$ have been subtracted out, leaving the flow contributing to OAM [22]. Propagation is shown through the beam waist ($z/z_{0x} = 0$) and into the far field ($\pm\infty$). The red arrows indicate the direction of spatiotemporal phase gradient $\nabla\Phi(x, \xi)$ and the red diagonals mark the boundary across which there is a phase jump of π. (b) Similar plots for spacetime-eccentric $l = 1$ STOVs with $\alpha = 0.5$ and $\beta_2 = 1, 0, -1$. For each row in (a) and (b), the value of $\langle L_y \rangle$ is shown in the $z = 0$ (centre) panels. Within each panel of (a) and (b), the pulse propagates right to left.

A physical explanation for half-integer STOV orbital angular momentum in vacuum is that electromagnetic energy density flow in the pulse frame is purely along $\pm x$, or along $\nabla_\perp$. In our coordinates, for $l = +1$, energy density flows along $-x$ in advance of the STOV singularity and along $+x$ behind it. Because $\beta_2 = 0$ or is negligible in vacuum or extremely dilute media, there is no energy flow along ξ. This is in contrast to a standard $LG_{space}^{0\pm1}$ mode, where electromagnetic energy density circulates clockwise or counterclockwise around the singularity. The dependence of $\langle L_y \rangle$ on β_2 can be interpreted as STOV-based transverse OAM being shared between a photon and a bulk medium STOV polariton.

We contrast our result with a recent calculation of STOV transverse OAM assuming zero dispersion ($\beta_2 = 0$) [24, 26], which yields $\langle L_y^B \rangle = l(\alpha + \alpha^{-1})/2$ for the intrinsic OAM. This result differs from the $\beta_2 = 0$ case of our Eq. (10): $\langle L_y \rangle = l\alpha/2$. It also conflicts with the direct computation from the $l = 1$ STOV fields in vacuum, $\langle \mathbf{r} \times (\mathbf{E} \times \mathbf{H}) \rangle_y = \alpha/2$ where $\mathbf{E}$ is the electric field of an $l = 1$ STOV and $\mathbf{H}$ is the corresponding magnetic field [27]. This is not surprising, since the operator for intrinsic transverse OAM written down in [24, 26], $L_y^B = -i\big(\xi\,(\partial/\partial x) - x(\partial/\partial\xi)\big)$, does not commute with

the space-time propagator H (that is, $[H, L_y^B] \neq 0$) and is therefore not conserved during propagation. Additionally, the result of [24, 26] worrisomely implies local superluminal and subluminal energy density flow along $\hat{\boldsymbol{\xi}}$ [22, 27].

Figure 4(a) shows plots of STOV intensity $\left|A_{\alpha=1}^{l=1}(x, y = 0, \xi; z)\right|^2$ and energy density flux $\mathbf{j}$, computed using Eq. (8), for $l = 1$, $\alpha = 1$ and $\beta_2 = 1$, 0.5, $0, -0.5, -1$, and Fig. 4(b) shows similar results for a spacetime-eccentric $l = 1$ STOV with $\alpha = 0.5$. For each row of Fig. 4, $\langle L_y \rangle = \frac{1}{2}(\alpha - \beta_2/\alpha)$ is a constant. The purely diffractive contributions to $\mathbf{j}$ have been subtracted out, leaving the flow contributing to OAM [22]. The red arrows show the direction of the spatiotemporal phase gradient $\nabla \Phi(x, \xi)$, and the red diagonals mark the boundary across which there is a phase jump of π. In the panels with the red diagonal, even though the phase winding has disappeared, $\langle L_y \rangle$ remains at the constant value of that particular row. It is seen that for a STOV propagating in a medium with $\beta_2 > 0$, the energy density flow exhibits a 'saddle' pattern with respect to the singularity, while for $\beta_2 < 0$ the flow is spiral and, as discussed for $\beta_2 = 0$, the flow is restricted to $\pm x$. Note that for $\beta_2 = 1$, where $\langle L_y \rangle = \frac{1}{2}(1 - \beta_2) \propto \int dx d\xi (\mathbf{r} \times \mathbf{j})_y = 0$ and OAM is shared equally by the electromagnetic and polariton response, $\mathbf{j}$ vanishes everywhere at $z = z_{0x}$.

A range of interesting behaviour is observed in Fig. 4, with the main points summarized as follows: (1) In normally dispersive materials ($\beta_2 > 0$), the directions of the OAM and the phase gradient do not always coincide; the phase winding direction can flip to maintain OAM conservation (see rows (i),(ii), and (vi)); (2) The phase winding can disappear, yet nonzero $\langle L_y \rangle$ remains (rows (iii) and (vi)); (3) A donut-shaped STOV launched in vacuum or dilute media does not stay together as a donut; the spatio-temporal energy flow component $\mathbf{j}_\perp$ forces the donut into spatiotemporally offset lobes (rows (iii) and (vii)); (4) For $\beta_2 \neq 0$, the near and far field intensity profiles are self-similar (all rows except (iii) and (vii)); (5) There exists a self-similar STOV mode with integer OAM for $\alpha = 1$ and $\beta_2 = -1$ (row (v)). Classically, this is visualized as balanced STOV energy flow along $\hat{\mathbf{x}}$ and $\hat{\boldsymbol{\xi}}$.

ACKNOWLEDGEMENTS

REFERENCES

[1] L. Allen, M. W. Beijersbergen, R. J. C. Spreeuw, and J. P. Woerdman, "Orbital angular momentum of light and the transformation of Laguerre-Gaussian laser modes," Phys. Rev. A **45**, 8185 (1992).

[2] H. He, M. E. J. Friese, N. R. Heckenberg, and H. Rubinsztein-Dunlop, "Direct observation of transfer of angular momentum to absorptive particles from a laser beam with a phase singularity," Phys. Rev. Lett. **75**, 826 (1995)

[3] B. M. Heffernan, S. A. Meyer, D. Restrepo, M. E. Siemens, E. A. Gibson, and J. T. Gopinath, "A fiber-coupled stimulated emission depletion microscope for bend-insensitive through-fiber imaging," Sci. Rep. **9**, 11137 (2019).

[4] G. A. Tyler and R. W. Boyd, "Influence of atmospheric turbulence on the propagation of quantum states of light carrying orbital angular momentum," Opt. Lett. **34**, 142 (2009).

[5] T. Doster and A. T. Watnik, "Laguerre–Gauss and Bessel–Gauss beams propagation through turbulence: analysis of channel efficiency," Appl. Opt. **55**, 10239 (2016).

[6] G. Vallone, V. D'Ambrosio, A. Sponselli, S. Slussarenko, L. Marrucci, F. Sciarrino, and P. Villoresi, "Free-space quantum key distribution by rotation-invariant twisted photons," Phys. Rev. Lett. **113**, 060503 (2004).

[7] N. Jhajj, I. Larkin, E. W. Rosenthal, S. Zahedpour, J. K. Wahlstrand, and H. M. Milchberg, "Spatiotemporal optical vortices," Phys. Rev. X **6**, 031037 (2016).

[8] A. Couairon and A. Mysyrowicz, "Femtosecond filamentation in transparent media," Phys. Rep. **441**, 47 (2007).

[9] L. Bergé, S. Skupin, R. Nuter, J. Kasparian and J.-P. Wolf, "Ultrashort filaments of light in weakly ionized, optically transparent media," Rep. Prog. Phys. **70**, 1633 (2007).

[10] F. Salehi, M. Le, L. Railing, M. Kolesik, and H. M. Milchberg, "Laser-Accelerated, Low-Divergence 15-MeV Quasimonoenergetic Electron Bunches at 1 kHz," Phys. Rev. X **11**, 021055 (2021).

[11] J. K. Wahlstrand, Y.-H. Cheng, and H. M. Milchberg, "Absolute measurement of the transient optical nonlinearity in N_2, O_2, N_2O, and Ar," Phys. Rev. A **85**, 043820 (2012).

[12] N. Jhajj, "Hydrodynamic and electrodynamic implications of optical femtosecond filamentation," Ph.D.dissertation (University of Maryland, 2017), https://drum.lib.umd.edu/handle/1903/19973, Chap. 5.

[13] S. Zahedpour, S. W. Hancock, and H. M. Milchberg, "Direct measurement of linearly imposed spatiotemporal optical vortices (STOVs)," in Frontiers in Optics + Laser Science APS/DLS, OSA Technical Digest (Optical Society of America, 2019), paper FW5F.5.

[14] S. W. Hancock, S. Zahedpour, A. Goffin, and H. M. Milchberg, "Free-space propagation of spatiotemporal optical vortices," Optica, **6** 1547 (2019).

[15] A. Chong, C. Wan, J. Chen and Q. Zhan, "Generation of spatiotemporal optical vortices with controllable transverse orbital angular momentum," Nat. Photonics **14**, 350 (2020).

[16] S. W. Hancock, S. Zahedpour, and H. M. Milchberg, "Transient-grating single-shot supercontinuum spectral interferometry (TG-SSSI)," Opt. Lett. **46**, 1013 (2021).

[17] S. W. Hancock, S. Zahedpour, and H. M. Milchberg, "Second-harmonic generation of spatiotemporal optical vortices and conservation of orbital angular momentum," Optica **8**, 594 (2021).

[18] S. W. Hancock, S. Zahedpour, and H. M. Milchberg, "Mode Structure and Orbital Angular Momentum of Spatiotemporal Optical Vortex Pulses," Phys. Rev. Lett. **127**, 193901 (2021).

[19] K. Y. Kim, I. Alexeev, and H. M. Milchberg, "Single-shot supercontinuum spectral interferometry," Appl. Phys. Lett. **81**, 4124 (2002).

[20] K. Dholakia, N. B. Simpson, and M. J. Padgett, "Second-harmonic generation and the orbital angular momentum of light," Phys. Rev. A **54**, R3742 (1996).

[21] R. W. Boyd, in Nonlinear Optics (Academic, 2008), pp. 69-133.

[22] S. W. Hancock, S. Zahedpour, and H. M. Milchberg, "Mode Structure and Orbital Angular Momentum of Spatiotemporal Optical Vortex Pulses," Phys. Rev. Lett. **127**, 193901 (2021).

[23] K. Y. Bliokh and F. Nori, Spatiotemporal vortex beams and angular momentum, Phys. Rev. A 86, 033824 (2012).

[24] K. Bliokh, "Spatiotemporal Vortex Pulses: Angular Momenta and Spin-Orbit Interactions," Phys. Rev. Lett. 126, 243601 (2021).

[25] A. Lotti, A. Couairon, D. Faccio, and P. Di. Trapani, "Energy-flux characterization of conical and space-time coupled wave packets," Phys. Rev. A **81**, 023810 (2010).

[26] K. Bliokh, "The Enigma of Orbital Angular Momentum of Spatiotemporal Vortex Pulses," https://arxiv.org/abs/2209.04371

[27] S.W. Hancock, S. Zahedpour, A. Goffin, and H.M. Milchberg, to be published.